Supplementary Information

Multiscale-Biomimetic Lamellar Hydrogel for Full-Thickness Corneal Replacement

Jingting Wang, Zhen Shi, Shang Yang, Zheng Shao, Mingxu Li, Fuyan Wang, Qingjun Zhou, Ting Wang, Long Zhao*, Weiyun Shi**

J. T. Wang, Z. Shi, Z. Shao, M. X. Li, F. Y. Wang, Q. J. Zhou, L. Zhao, W. Y. Shi
Eye Institute of Shandong First Medical University, State Key Laboratory Cultivation Base, Shandong Key Laboratory of Eye Diseases, Qingdao Key Laboratory of Ophthalmic Implantable and Interventional Medical Materials, School of Ophthalmology, Shandong First Medical University, Qingdao 266071, P. R. China.
*Corresponding authors
E-mail: weiyunshi@163.com (W. Y. Shi); zhaolong@email.sdfmu.edu.cn (L. Zhao)

S. Yang
Shandong Medical and Pharmaceutical University, Yantai 264003, China

*T. Wang
Eye Institute of Shandong First Medical University, Eye Hospital of Shandong First Medical University (Shandong Eye Hospital), State Key Laboratory Cultivation Base, Shandong Key Laboratory of Eye Diseases, School of Ophthalmology, Shandong First Medical University, Jinan 250021, P. R. China
E-mail: wting@sdfmu.edu.cn (T. Wang)

Table of Contents

1. Methods.....3
Materials and sources.....3
Preparation of control materials.....3
General physical characterizations.....5
2. Tables and Figures.....15
Table S1. Summary of key clinical and preclinical studies on the therapeutic outcomes of synthetic artificial corneal substitutes.....15
Table S2. Summary of key biophysical properties of corneal substitutes.....17
Table S3. Mechanical properties of different corneal substitute materials.....19
Table S4. Clinical scoring of corneal opacity.....21
Table S5. Antibody information.....21
Fig. S1. Morphology of PVA hydrogels by different freezing methods.....22
Fig. S2. Dual temperature gradient of 2DP.....23
Fig. S3. Characterization of 2DP lamellar spacing.....24
Fig. S4. Tunable lamellar structure of 2DP hydrogels.....24
Fig. S5. Contribution of GelMA to hierarchical lamellar structure of 2DPG-CA.....25
Fig. S6. Effect of omnidirectional confined assembly on hydrogel crystallinity..25
Fig. S7. Optical transmittance of 2DPG-CA.....26
Fig. S8. Hierarchical lamellar structural parameters of 2DPG-CA.....26
Fig. S9. Surface morphology of 2DPG-CA under varying pre-strain.....27
Fig. S10. Inter-groove spacing of 2DPG-CA vs. SFTC.....27
Fig. S11. 2D WAXS and SAXS patterns of 2DP-CA and GelMA.....28
Fig. S12. Polarized optical microscopy (POM) characterization of SFTC.....28
Fig. S13. WAXS characterization of domain sizes.....29
Fig. S14. FTIR of SFTC hydrogel interactions.....29
Fig. S15. Hydration stability of SFTC.....30
Fig. S16. Mechanical characterization of SFTC.....31
Fig. S17. In-plane isotropic mechanical performance of SFTC.....31
Fig. S18. Isotropic suture retention of SFTC.....32
Fig. S19. Mechanics modelling for suture resistance of SFTC.....33
Fig. S20. Notch insensitivity of SFTC.....33
Fig. S21. Suture retention performance of SFTC.....34
Fig. S22. Quantitative cell viability analysis.....34
Fig. S23. Asymmetric Cell Adhesion of SFTC.....35
Fig. S24. Asymmetric fibrin microsphere adhesion of SFTC.....35
Fig. S25. Functional visual recovery performance of SFTC.....36
Fig. S26. Proteomic analysis of SFTC and PVA-C transplant groups.....37
Fig. S27. SFTC for skin regeneration.....37
3. References:.....38

1. Methods

Materials and sources

All reagents were of analytical grade without further purification. Polyvinyl alcohol (PVA) powder (*Mw*: 146000–186000, >99% hydrolyzed), human type IV collagen, collagenase, 1-[3-(dimethylamino) propyl]-3-ethylcarbodiimide methiodide (EDCM), N-hydroxysuccinimide (NHS) and riboflavin were purchased from Sigma-Aldrich (Missouri, USA). Gelatin methacryloyl (GelMA，60% substitution) and sodium phenyl (2,4,6-trimethylbenzoyl) phosphinate (NAP) were supplied by Lingel Technology Co., Ltd. (Shanghai, China). Type I porcine dermal atelocollagen was obtained from MSBio, Inc. (Seongnam, Republic of Korea). Laminin was sourced from Unicollagen Biomedicine Co., Ltd. (Jiangsu, China). Transglutaminase was provided by Yuanye Biotechnology Co., Ltd. (Shanghai, China). Phosphate-buffered saline (PBS), 4% paraformaldehyde, and bovine serum albumin were purchased from Solarbio Science & Technology Co., Ltd. (Beijing, China).

SV40-immortalized human corneal epithelial cells (HCEC; catalog No. CRL-11135) were purchased from the American Type Culture Collection (ATCC, Manassas, VA, USA). Telomerase-immortalized human corneal stromal cells (HCSCs) were a generous gift from Dr. James Jester (University of California, Irvine, CA, USA). Both cell lines were cultured in Dulbecco's modified Eagle's medium/Nutrient Mixture F12 (DMEM/F12; Sigma-Aldrich, St. Louis, MO, USA) supplemented with 10% (v/v) fetal bovine serum (FBS; Thermo Fisher Scientific, Waltham, MA, USA) at 37 °C and 5% CO_2.

Preparation of control materials

1DP hydrogels. A 5% (w/v) PVA solution was cast into polytetrafluoroethylene (PTFE)

molds with a copper base, with the copper base directly contacting dry ice for freezing at −80 °C for 12 h, followed by thawing at room temperature with 55% relative humidity and 24 °C for another 12 h.

RP hydrogels. A 5% (w/v) PVA solution was cast into a glass mold, and then frozen at −80 °C for 12 h, followed by thawing at room temperature for another 12 h.

2DP-CA hydrogels. The as-prepared 2DP hydrogels (as described in the Experimental Section of the main text) were mounted on a custom-fabricated corneal mold with a 44 D curvature, prestrained by 10%, secured with an annular clamp, and air-dried for 48 h at 24 °C and 20% relative humidity.

2DPG-RA hydrogels. The as-prepared 2DPG hydrogels (as described in the Experimental Section of the main text) were photo-crosslinked under 365-nm UV irradiation (100 $mW \cdot cm^{-2}$) for 1 min., and air-dried for 48 h.

1DPG-CA hydrogels. As-prepared 1DP hydrogels were infiltrated with GelMA prepolymer (as described in the Experimental Section of the main text) to yield 1DPG, which was then uniaxially stretched by 10% along the aligned fiber orientation, photo-crosslinked under UV irradiation, and air-dried for 48 h.

PVA-C hydrogels. PVA-C hydrogels were fabricated via a modified freeze-thaw protocol adapted from a previous report.[1] Briefly, a 10 wt% PVA solution was prepared by dissolving the polymer in deionized water and dimethyl sulfoxide (DMSO) (2:8, v/v), heated at 140 °C for 2 h, cast into a glass mold, and then subjected to three freeze-thaw cycles (12 h freezing at −80 °C, 12 h thawing per cycle), followed by thorough rinsing with deionized water to remove residual solvent.

Gel-C hydrogels. A 20% (w/v) GelMA prepolymer solution containing 0.25% (w/v)

sodium phenyl (2,4,6-trimethylbenzoyl) phosphinate (NAP) was cast onto a mold and photo-crosslinked under 365-nm UV irradiation for 1 min.

Col-C hydrogels. Col-C was prepared according to the standardized manufacturing protocol for clinical collagen corneal stromal substitutes.[2] Briefly, freeze-dried porcine type I atelocollagen was dissolved in sterile 1× PBS to prepare a 10% (w/v) collagen solution, EDCM, NHS and riboflavin were added as crosslinkers at 1% (w/v) each. The solution was cast onto a mold and cured at room temperature. After rinsing with PBS, samples were further subjected to secondary UVA-riboflavin photochemical crosslinking.

General physical characterizations

Scanning electron microscopy (SEM). Samples were fixed in 2.5% (v/v) glutaraldehyde at 4 °C for 12 h, dehydrated through a graded ethanol series, critical-point dried with liquid CO_2, cryofractured in liquid nitrogen, and sputter-coated with a ~5 nm gold layer (Leica ACE200). Internal architecture and surface morphology were imaged by SEM (VEGA3, TESCAN, Brno, Czech Republic) at an accelerating voltage of 20 kV. All structural parameters were quantified from SEM images using ImageJ software (NIH, Bethesda, MD, USA). For each parameter, 200 random measurements were collected from 3 independently fabricated samples (n = 3).

Differential scanning calorimeter (DSC). Samples were crosslinked with excess glutaraldehyde prior to drying, hermetically sealed in aluminum pans, and characterized by DSC on a Discovery DSC25 (TA Instruments, New Castle, DE, USA) under nitrogen atmosphere (35 mL/min) from 10 to 300 °C at a heating rate of 20 °C/min.

The degree of crystallinity (X_c) of the PVA component was calculated by the following Equation (1):

$$X_C\% = \left[\frac{\Delta H_m}{(w \cdot \Delta H_m*)}\right] \times 100\% \quad (1)$$

here ΔH_m is the melting enthalpy of PVA, w is the mass fraction of PVA in the dried hydrogel, ΔH_m^* is the theoretical melting enthalpy of 100% crystalline PVA, taken as 138.6 J g^{-1}.

X-ray scattering characterization. Freeze-dried samples were characterized by X-ray scattering at ambient temperature (22 °C). Wide-angle X-ray scattering (WAXS, transmission mode) and small-angle X-ray scattering (SAXS) measurements were performed with Cu Kα radiation on a customized microfocus X-ray diffraction system (WAXS; Xenocs SA, France) and a Xeuss 1.0 system (SAXS; λ = 0.154189 nm), respectively, with the X-ray tube operated at 50 kV and 0.6 mA. Two-dimensional scattering patterns were processed with Fit2D to extract azimuthal intensity profiles, with data plotting and quantification performed in Origin software (Origin Pro 2024b, 10.1.0.178, Origin Lab, MA, USA).

The intermolecular spacing (L) of the hydrogel networks was derived from WAXS profiles via the Bragg equation (2):

$$L = \frac{\lambda}{2\sin\theta} \quad (2)$$

The ordered domain sizes (d) were quantified from one-dimensional intensity 2θ scattering profiles extracted from WAXS patterns using Scherrer's equation (3):

$$d = \frac{k\lambda}{\beta\cos\theta} \quad (3)$$

where β is the full width at half maximum of the primary diffraction peak, and $k = 0.89$ is adopted as the standard dimensionless shape factor for lamellar crystallites.

The interdomain periodic distance (D) of hydrogel samples of PVA material was quantified by the one-dimensional scattering curve of corrected scattering intensity (Iq^2) versus scattering vector (q) obtained by 2D SAXS patterns, as follows (4, 5):

$$D = \frac{2\pi}{q} \quad (4)$$

$$q = \frac{4\pi(\sin\theta)}{\lambda} \quad (5)$$

Fourier transform infrared (FTIR) spectra. Samples were vacuum-dried to constant

weight at 50 °C. FTIR spectra were acquired on a Bruker Alpha P spectrometer with a diamond ATR accessory. Spectra were recorded with 24 scans at 4 cm^{-1} resolution over 4000–500 cm^{-1}.

Polarizing optical microscopy (POM) characterization. POM measurements were performed on a Nikon LV100POL system equipped with a 530 nm sensitive tint plate and a Berek compensator.

Transparency and haze characterization. Macroscopic sample transparency was qualitatively assessed via digital photography with a HUAWEI Pura 70 Pro smartphone (Huawei, Shenzhen, China), while optical transmittance and haze were measured from 380 to 800 nm on a Lambda 950 UV-Vis spectrophotometer (PerkinElmer, Waltham, MA, USA) with an integrating sphere.

The light transmittance (T_t) and the haze (H) were calculated by the following Equations (6, 7):

$$T_t = \frac{T_2}{T_1} \times 100\% \quad (6)$$

$$H = \left[\left(\frac{T_4}{T_2} - \frac{T_3}{T_1}\right)\right] \times 100\% \quad (7)$$

where T_1 is the incident light flux, T_2 is the total transmitted light flux through the sample, T_3 is the instrument background scattered light flux, T_4 is the total scattered light flux from both the instrument and the sample.

Water content test. Samples were weighed at equilibrium swelling (W_0), then dried to constant weight at 40 °C in a forced convection oven (GFL125A, Blabotery, China) to obtain the dry weight (W_d). Water content was calculated using Equation (8):

$$\text{Water content}\% = \frac{W_0 - W_d}{W_0} \times 100\% \quad (8)$$

Porosity measurement. Freeze-dried samples were weighed for dry mass (W_d), then vacuum-infiltrated in absolute ethanol, and reweighed for ethanol-saturated wet mass

(W_w). Apparent total volume (V_t) was determined via water displacement. Porosity (P_r) was calculated according to the following Equation (9):

$$P_r\% = \frac{W_w - W_d}{V_t \cdot \rho} \times 100\% \quad (9)$$

where ρ is the density of ethanol at 25 °C, with a value of 0.789 g mL^{-1}.

Oxygen permeability (Dk). Measurements were made using the Fatt polarographic method in accordance with ISO 18369-4:2006 on a Model 201T oxygen permeameter (Createch Rehder Development Co., Livermore, CA, USA) at 35 °C under a fully humidified atmosphere.

Permeability performance test. Permeation measurements were conducted using Franz diffusion cells. Glucose and lactic acid concentrations were quantified with a GOPOD assay kit (JL-T104) and a lactic acid assay kit (JL-T1068), respectively. Absorbance was measured on a UV-Vis spectrophotometer (Molecular Devices, Silicon Valley, CA, USA) at 520 nm and 450 nm, with calculations based on standard curves ($R^2 > 0.999$).

The steady-state permeation flux (J) was calculated using Equation (10):

$$J = \frac{\Delta M}{A \cdot \Delta t} \quad (10)$$

where ΔM is the mass of permeant accumulated in the receiver chamber during the time interval Δt (μg), A is the effective diffusion area of the membrane (cm^2), and Δt is the time interval (s).

Permeability Coefficient (P) was calculated using the following Equation (11):

$$P = \frac{J}{C_0} \quad (11)$$

where C_0 is the initial concentration in the donor chamber.

Enzyme resistance assay. Samples were weighed for initial mass (W_0), then incubated in 100 U mL^{-1} collagenase solution at 37 °C for 7 days. Residual mass (W_t) was

247 measured at predetermined intervals, and residual mass percentage was calculated
248 using Equation (12):

249 $$\text{Residual mass}\% = \frac{W_t}{W_0} \times 100\% \quad (12)$$

250

251 **Swelling behavior analysis.** Samples were weighed for initial mass (W_0), then
252 immersed in physiological saline at 37 °C for 5 days and weighed daily (W_t). Swelling
253 ratio was calculated using Equation (13):

254 $$\text{Swelling ratio}\% = \frac{W_t - W_0}{W_0} \times 100\% \quad (13)$$

255

256 **Mechanical testing.** Tensile testing was conducted on a universal testing machine
257 (AGS-X-10KN, Shimadzu, Kyoto, Japan) at a stretching speed of 10 mm·min^{-1}. Strain
258 was defined as the ratio of the change in length to the initial length, and stress was
259 calculated by dividing the applied force by the cross-sectional area of the samples.
260 Young's modulus was determined from the slope of the initial linear region of the
261 stress–strain curve, and toughness was calculated by integrating the area under the
262 entire stress–strain curve to evaluate the hydrogels' energy absorption capacity.

263

264 **Suture retention strength.** To measure the suture strength, Nylon 5/0 was used to
265 thread through one end of a gel strip at 5 mm from the edge of the test sample. The free
266 ends of each suture were fixed on clamps of a universal testing machine. Tests were
267 conducted at a rate of 1 mm min^{-1} until failure, and maximum breaking force (F_{max})
268 and the failure mode were recorded for analysis. The suture retention strength (σ_{sr})was
269 calculated using Equation (14):

270 $$\sigma_{sr} = F_{max}/(2dt) \quad (14)$$

271 where d is the diameter of applied suture, t is the thickness of tested materials.

272

273 **Burst tests.** Samples were mounted on an artificial anterior chamber (Moria, Paris,
274 France) connected to a syringe pump (LongerPump, Hebei, China) and a pressure
275 monitor (MedLab-U/4C501H, Shanghai, China). PBS was injected at 5 μL·s^{-1} until

sample rupture. Maximum burst pressure was recorded.

Finite element analyses (FEA). FEA was performed using ABAQUS 2018 (SIMULIA, Dassault Systèmes, France). Specifically, key mechanical parameters including Young's modulus, Poisson's ratio and fracture energy were assigned to each component. Boundary conditions and tensile loads were configured to replicate the in vitro suture tear test, and stress distribution and crack propagation behavior were subsequently compared.

Tear fatigue threshold test. The tear fatigue threshold was determined via single-edge notched tension on pre-notched samples (20 mm× 10 mm× 0.5 mm, with a pre-crack length of 2 mm). Cyclic tensile tests were conducted across a series of maximum stretch ratios (λ_{max}). Crack length and propagation morphology were monitored at specified cycles under zero load using a digital microscope (AM4815ZT, Dino-Lite). The relationship between crack growth rate per cycle (dc/dN) and maximum energy release rate (G_{max}) was established by gradient adjustment of λ_{max}. The fatigue threshold energy release rate (G_{th}), defined as the G_{max} value corresponding to dc/dN = 0, was obtained by linear extrapolation of the fitted curve to the x-axis.

Fatigue performance test. Samples with identical dimensions and a 2 mm pre-notch consistent with the fatigue threshold tests, were used for long-term fatigue evaluation. Tests were carried out on a U-type tensile testing system (CellScale, Canada) equipped with a 25 °C water bath and a 10 N load cell. Displacement-controlled cyclic tensile loading was applied at a crosshead speed of 10 mm·min^{-1}, with a fixed maximum stretch ratio (λ = 2.0) for 10,000 consecutive cycles. Real-time force and displacement signals were recorded throughout the test to assess the mechanical stability and fatigue resistance of the hydrogels under sustained crack tip loading.

Live-dead staining. HCECs and HCSCs were separately seeded in 12-well plates at 1

× 10^5 cells per well and allowed to adhere for 12 h. Sterilized SFTC hydrogels were then added to the wells for 48 h of co-culture. The cells cultured with an equal volume of fresh complete medium served as the control. After incubation, cells were stained with a Live/Dead Cell Double Staining Kit (KTA1001, Abbkine, Wuhan, China) and imaged under an inverted fluorescence microscope (Eclipse Ti-U, Nikon, Tokyo, Japan). Cell viability was quantified via ImageJ software from randomly selected fields of view. Cell proliferation was monitored daily using the Cell Counting Kit-8 (CCK-8; Dojindo Laboratories, Kumamoto, Japan) according to the manufacturer's protocol.

Cell migration assay. HCECs and HCSCs were separately seeded in 6-well plates at 5 × 10^5 cells per well and cultured to 80–90% confluence. A scratch was made in the cell monolayer using a sterile 200-microl pipette tip. The cells were cultured in complete medium pre-conditioned with sterile SFTC hydrogels, with fresh complete medium serving as control. Phase-contrast images of the scratch were acquired at 0 h, 24 h and 48 h post-scratch. The residual scratch area was quantified using ImageJ software to calculate the wound closure rate.

Fibrin microsphere adhesion test. CY3.5-labeled fibrin microspheres (10 μm) were dispersed in pH 7.4 PBS (2.5% v/v). SFTC samples were incubated in the microsphere suspension at 37 °C for 10 min in the dark, followed by PBS rinsing. Adherent microspheres on epi- and endo-surfaces were imaged via laser scanning confocal microscopy (LSM 880, Carl Zeiss, Germany), and adherent microsphere density was quantified using ImageJ software.

RNA sequencing. HCECs were seeded on SFTC hydrogel epi-surfaces (experimental group) or 6-well plates (control) at 1 × 10^5 cells per well and cultured for 7 days. Total RNA was extracted with TRIzol reagent (Invitrogen, Thermo Fisher Scientific, Carlsbad, CA, USA). Differential gene expression analysis was conducted with the DESeq2 R package, and differential expression screening was performed with

thresholds of $|\log_2 FC| \geq 1$ and adjusted $p < 0.05$. Gene Ontology enrichment analysis was performed using the clusterProfiler R package. Gene Set Enrichment Analysis was additionally carried out with GSEA v3.0 using gene sets from the Molecular Signatures Database (MSigDB v6.1).

Rabbit penetrating keratoplasty in burn-perforation model. Healthy male New Zealand White rabbits (5–6 months old, n = 4) were anesthetized via intramuscular injection of ketamine (40 $mg \cdot kg^{-1}$) and chlorpromazine (20 $mg \cdot kg^{-1}$). A full-thickness corneal thermal burn–perforation model was established: a 4 mm central corneal area was cauterized for 30 s to form a uniform opaque lesion, followed by central perforation with a 23G needle.

For penetrating keratoplasty, the 5 mm lesioned cornea was excised via trephination, and a 5.25 mm-diameter SFTC graft was implanted into the recipient bed and secured with twelve interrupted 10-0 nylon sutures. Allogeneic rabbit corneas, PVA-C hydrogels, and conjunctival flaps served as control grafts. Conjunctival flap coverage was conducted in accordance with standard clinical practice.[3] Postoperative care included topical application of tobramycin dexamethasone ophthalmic ointment (Alcon Couvreur N.V., Puurs, Belgium) twice daily for 7 days, followed by tobramycin dexamethasone eye drops three times daily until postoperative day 28.

Clinical assessments. Corneal clarity, neovascularization, and inflammation were evaluated via slit-lamp biomicroscopy (SL-D701, Topcon, Tokyo, Japan). Corneal epithelial integrity was assessed via sodium fluorescein staining, with residual defect areas quantified via ImageJ software. The semiquantitative Preclinical Ocular Toxicology Scoring (SPOTS) system was used to grade corneal opacity and vascularization (detailed criteria in Table S4).[4] Cross-sectional images and pachymetry maps were obtained via anterior segment optical coherence tomography. Intraocular pressure was measured with a rebound tonometer (TonoVet, West Jordan, UT), and in

vivo corneal stromal microarchitecture was examined via HRT3 confocal microscopy with the Rostock Corneal Module (RCM; Heidelberg Engineering, Germany).

Foraging behavior assessment. Foraging behavior was tested on postoperative day 28. Rabbits (n = 4) were acclimated to dried Timothy hay for 3 consecutive days and deprived of food and water for 24 h prior to testing. The contralateral healthy eye was occluded with surgical adhesive tape. Printed hay targets and neutral distractors were affixed to the enclosure walls, with positions randomized across trials. Each rabbit was released from a fixed starting point, and target localization latency was recorded within 5 min. Foraging trajectories were video-recorded (HUAWEI Pura 70 Pro smartphone), and average path length before target localization was quantified via ImageJ software.

Histological staining. Hematoxylin and eosin (H&E) staining was performed following the manufacturer's protocol (Vector Laboratories, Burlingame, CA, USA). For immunofluorescence staining, samples were fixed with 4% (w/v) paraformaldehyde for 15 min, permeabilized with 0.1% (v/v) Triton X-100 for 10 min, and blocked with 5% (w/v) bovine serum albumin for 1 h at room temperature. Primary antibodies (Table S5) were incubated overnight at 4 °C, followed by species-matched fluorophore-conjugated secondary antibodies for 1 h in the dark. After DAPI counterstaining and antifade mounting, fluorescence images were acquired with a Zeiss LSM 880 confocal microscope (Carl Zeiss, Oberkochen, Germany), with quantification performed using ZEN Lite 3.8 (Carl Zeiss).

Proteomic analysis. Corneal tissues (n = 3) were cryogenically pulverized in liquid nitrogen, followed by protein extraction, centrifugation, and concentration quantification via the bicinchoninic acid assay. Equal protein amounts were trypsin-digested per standard protocols. Peptide separation was performed using an EASY-nLC™ 1200 nanoflow system (Thermo Fisher Scientific, USA) coupled with a timsTOF Pro mass spectrometer (Bruker Daltonics) equipped with an Easyspray ion

source. Chromatographic separation was performed on a reversed-phase C18 column (25 cm × 75 μm) using a 90-min linear gradient. MS/MS data were processed using MaxQuant (v2.1.3.0) against the *Oryctolagus cuniculus* UniProtKB database (2023.02) and differentially expressed proteins ($|\log_2 FC| > 1$, $p < 0.05$) underwent GO enrichment analysis.

Skin replacement model in mice. Mice were anesthetized via intraperitoneal injection of 0.6% sodium pentobarbital at a dose of 40 mg/kg. A 10 mm full-thickness circular skin defect was generated on the dorsum via trephination. A 10 mm SFTC hydrogel was applied to the defect and secured with interrupted 6-0 nylon sutures. Postoperatively, Mupirocin ointment (Sino-American Smithkline) was topically applied and then covered with dry dressings, with wound appearance monitored via slit-lamp photography.

Statistical analysis. All statistical analyses were performed using GraphPad Prism 10 (GraphPad Software, San Diego, CA, USA) and Origin Pro 2024b (version 10.1.0.178; OriginLab Corporation, Northampton, MA, USA). Each experiment was independently repeated at least three times unless otherwise specified, and data are presented as mean ± standard deviation (SD). Comparisons between two groups were performed using a two-sided unpaired Student's t-test. For comparisons of three or more groups, one-way analysis of variance (ANOVA) followed by Tukey's post hoc multiple comparisons test was applied. A P value < 0.05 was considered statistically significant.

2. Tables and Figures

Table S1. Summary of key clinical and preclinical studies on the therapeutic outcomes of synthetic artificial corneal substitutes.

Device	Core material	Optical zone diameter	Clinical status	Main complications	Ref.
Boston Type 1 KPro	PMMA, titanium	3.35–3.7 mm	FDA approved (1992); global standard	RPM (36.6%); secondary glaucoma (39.3%); sterile keratolysis/melting (14.5%)	[5, 6]
Boston Type 2 KPro	PMMA, titanium	~3.5 mm	FDA approved; reserved for severe dry/cicatrizing ocular surface disease	RPM (60.4%); glaucoma onset/progression (~1/3); tarsorrhaphy revision (52.1%); initial device retention 50.0%	[7]
AlphaCor	PHEMA	~4.5 mm	Approved, withdrawn 2016; limited use	Stromal melting (26.4–60%); optic deposits/haze; RPM (20%); 3-yr retention ~42%	[8, 9]
Modified OOKP (osteo-odonto-KPro)	PMMA	4.0–5.0 mm	Clinical; end-stage salvage	Osteo-dental plate resorption (14.4%); endophthalmitis (7.7%); glaucoma; retinal detachment (6.4%)	[10]
Mihe (MIOK) KPro (China)	PMMA, titanium	2.5 mm	NMPA approved (2021); for bilateral end-stage corneal blindness	Device retention 97.2% fibrovascular tissue overgrowth (14.3%); macular edema (14.3%); residual cortical lens (11.4%); newly acquired glaucoma (8.57%); RPM (2.86%)	[11]

Collar-button KPro (c-bKPro, China)	PMMA, titanium	3 mm	NMPA approved; end-stage corneal blindness	RPM (16.1%); persistent epithelial defect (16.1%); macular edema (12.9%); glaucoma (12.5%); sterile corneal melting (6.5%)	[12]
Aurolab KPro (India)	PMMA, titanium	3.5 mm	Clinical; aphakic/pseudophakic options	5-yr anatomical retention 43.8%; functional recovery 35.0%; postoperative extrusion (12.5%); glaucoma (59%)	[13, 14]
MICOF (Russia)	PMMA, titanium	2.5 mm	Clinical; severe ocular surface disease	RPM (45.9%); glaucoma (11.8–60%); melting (40%); 3-yr retention 78.8%	[15, 16]
Lucia KPro	PMMA, titanium	3.5 mm	FDA approved (2019)	Anatomic retention 95.83%; glaucoma (37.5%); RPM (33.3%)	[17, 18]
CorNeat KPro	PMMA, carbonated polyurethane	~6.5 mm;	Phase I/II trial; limited clinical use	First-in-human (1 eye): local nasal conjunctival retraction. Rabbit (8 eyes, 6 mo): retention 87.5%	[19, 20]
BioKpro III	PDMS, PTFE	5.0 mm	Early clinical, exploratory	Retention (14.3%) over 18–48 mo; extrusion (85.7%), RPM (42.9%)	[21]
Porous integrating KPro	PFA，ePTFE	Anterior optic 4.60 mm, posterior 4.28 mm	Lab exploration; limited cases	Optic surface does not support epithelialization	[22]
***ht*-HAH**	Hydrothermally-treated PVA	6.0 mm	Preclinical, animal study	Does not support epithelial regeneration.	[23]

Abbreviations: KPro, keratoprosthesis; PMMA, poly(methyl methacrylate); PHEMA, poly(2-hydroxyethyl methacrylate); PVA, poly(vinyl alcohol); ht-HAH, hydrothermally-treated hydrophobic-association hydrogel; PDMS, poly(dimethylsiloxane); PTFE, polytetrafluoroethylene; ePTFE, expanded polytetrafluoroethylene; PFA, perfluoroalkoxy alkane; RPM, retroprosthetic membrane; FDA, U.S. Food and Drug Administration; NMPA, National Medical Products Administration; OOKP, osteo-odonto-keratoprosthesis; MIOK, Mihe keratoprosthesis; c-bKPro, collar-button keratoprosthesis; MICOF, Moscow Eye Microsurgery Complex keratoprosthesis; LSCD, limbal stem cell deficiency.

Table S2. Summary of key biophysical properties of corneal substitutes.

Corneal substitutes	Subtype	Transparency (%)	Epi-healing	Sutureability	Modulus (MPa)	Swelling ratio (%)	PKP suitability	Optical stability in vivo	Anti-degradation
Acellular scaffold	Acellular cornea	60–80[24]	7–14 days[25, 26]	Interrupted suture[25, 27]	0.95–10[24, 26, 28]	300–600[24, 29]	Mostly unsuitable[25, 26, 30]; PKP requires dual-crosslinked hydrogel reinforcement[31]; PKP requires human endothelial cells[32]	Corneal edema and opacification at day 14[33]	<10% residual mass (day 7; 100 U mL^{-1} collagenase)[34]
	Acellular non-corneal tissues	72–93[35, 36]; opaque[37]	14 days[33]	Interrupted suture[33]	56–402[35]; 8[33]	Limited or moderate swelling[33, 38]	Mostly unsuitable[37, 39]; requires structural reinforcement[33]	Opacity at day 21[40]	94% residual mass (day 5; 50 U mL^{-1} collagenase)[33]
Biohydrogel cornea	Patch	80–98[41, 42]	14–28 days[43, 44]	Interrupted suture;[43, 45] partially relies on adhesion[44] or overlay sutures[29]	0.8–16[46, 47]	10–60[48]	Mostly unsuitable[2, 43, 49]; limited use for 1 mm perforation[34]	Stromal haze at 3–6 months[50]	Complete degradation time 35 h (0.5 U mL^{-1} collagenase)[51]
	Injectable	80–99[52, 53]	7–14 days[54]	Suture intolerance[55]	0.009–0.3[52, 54]	Limited swelling[55]	Mostly unsuitable[56]; limited use for 1-mm-	Opacity[55]	Degradation in 14–28 days in vivo[53, 56]

							diameter perforation repair[55, 57]		
Keratoprosthesis	Hard artificial cornea	>80[58]	Unable[58]	Reliance on donor skirt[5]	1700–5300[33, 58]	Limited swelling[58]	3-mm-diameter optical zone restoration[5]	Optic RPM[59]	PMMA resisted collagenase degradation[33]
	Soft artificial cornea	>90[23]	Unable[9]	Interrupted suture[23]	0.2–5.3[1, 60]	Limited swelling[23]	4.5-mm-diameter optical zone restoration[9]	Optic depositions[8]	PHEMA resisted collagenase degradation[61]
Cornea		78–85[44, 62]	2–8 days[63]	Interrupted suture	0.67–2.5[34, 64]	~20 for 7 days in vivo[65]	Donor needs healthy endothelium	Edema from endothelial decompensation[66]	Degradation time 96 h (100 U mL^{-1} collagenase)[33]
SFTC (this work)		81.5 ± 0.7[a)]	6 ± 2.2[a)] days	Interrupted suture	0.8 ± 0.02[a)]	6.7 ± 1.2[a)]	5-mm-diameter optical zone restoration	Stable	46.2 ± 2.4%[a)] residual mass for 7 days (100 U mL^{-1} collagenase)

[a)] n = 3 independent samples; data are presented as the mean ± SD.

Table S3. Mechanical properties of different corneal substitute materials.

Corneal substitutes	Main materials	Methods	Modulus (MPa)	Water content (%)	Toughness (MJ m^{-3})	Suture resistance	Ref.
Collagen	RHC	CMC/NHS crosslinking	16.34 ± 2.7	86.6 ± 0.15	0.1–0.2	Running suture	[47]
	Collagen/ECM	Collagen vitrification /β-cyclodextrin assembly	~7–11	85	0.05	0.294 N (load)	[64]
	Collagen	Glycerol-mediated assembly	1.97	81.6	~0.6[a)]	~50 g (load)	[43]
	Collagen/Chitosan	Hybrid cross-linking	0.838	90.0	~0.03[a)]	Overlying suture	[46]
	Collagen	Polyrotaxane aldehyde crosslinking	1.59	81.4	~0.02[a)]	0.46 N (load)	[67]
	Collagen	Dendrimer/EDC/NHS crosslinking	1.4–5.3	~80[a)]	N/A	5.5 g (load)	[42]
GelMA	GelMA/OCS	Visible light crosslinking	0.061	83	~0.025[a)]	Suture intolerance	[68]
	GelMA	UV crosslinking	0.005	>95	N/A	Suture intolerance	[57]
	GelMA	Visible light crosslinking	0.224	85–86	0.03–0.25[a)]	Suture intolerance	[54]
	GelMA/F127DA	UV crosslinking	0.02	>90	0.08–0.1	Suture intolerance	[56]
	GelMA	UV crosslinking	0.009–0.03	>80	0.001–0.05[a)]	Suture intolerance	[52]
Gelatin	Gelatin/alginate	Electrospinning	0.45	Limited	0.14	N/A	[69]
	Gelatin/alginate	Electrospinning/EDC/NHS	3.21	Limited	~3.96	Crack- resistant	[70]
	Collagen/gelatin/alginate	EDC/NHS crosslinking	0.06–0.08	>90	0.2–1.7×10^{-2}	Suture intolerance	[71]
	Gelatin glycidyl methacrylate	Visible light crosslinking	1.04	>80	1.26	0.14 N (load)	[68]
Silk	Silk	Ethanol soaking/drying	11 ± 3.2	48	~0.09	19.8 ± 2.89 g (load)	[72]
	Silk/collagen	EDC/NHS crosslinking	4.51	76	~0.2[a]	10 g (load)	[45]
	Silk/GelMA	UV crosslinking	0.32	59 ± 15	1.3 ± 0.4	Suture intolerance	[73]
PVA	PVA/Collagen	Electrospinning	~3[a)]	Limited	~1.2[a)]	N/A	[74]

	PVA/SF/n-HA	Genipin/freeze-thawing	0.2–0.3[a)]	69–71	0.5–0.6[a)]	N/A	[60]
	PVA	Arrested phase separation	~0.69	~70–80	0.1	0.53 MPa	[23]
PMMA	PMMA	N/A	5.3×10^3	Limited	~0.376[a)]	N/A	[58]
	PMMA	N/A	$2.9–3.5\times10^3$	Limited	N/A	N/A	[75]
	PMMA	N/A	1.7×10^3	Limited	~0.07	N/A	[33]
PCL	PCL	Electrospinning	7.5	Limited	~3.6[a)]	N/A	[1]
	PCL	Direct writing	~13.3	85.26 ± 0.94	~0.77[a)]	Interrupted suture	[76]
	Gelatin/PCL	Electrospinning	15.5	Limited	~0.15[a)]	N/A	[77]
Cornea	Pig cornea	–	0.67	~80	0.52	Interrupted suture	[34]
	Rabbit cornea	–	~2.5	~80	~0.78[a)]	Interrupted suture	[64]
	Human cornea	–	2.47	~80	0.48	Interrupted suture	[33]
SFTC (this work)	GelMA/PVA	Bidirectional freeze-casting/omnidirectional in-plane confined drying	0.8 ± 0.02[b)]	79.5 ± 1.3[b)]	1.01 ± 0.16[b)]	23.3 ± 1.3[b)] MPa	

[a)] The values are calculated from mechanical data reported in the cited references; [b)] n = 3 independent samples; data are presented as the mean ± SD.

Abbreviations: N/A, Data not reported in the original literature; RHC, Recombinant human collagens; F127DA, Pluronic F127 diacrylate; PCL, poly(ε-caprolactone); EDC, 1-Ethyl-3-(3-dimethylaminopropyl) carbodiimide hydrochloride; NHS, N-hydroxysuccinimide; CMC, N-Cyclohexyl-N′-(2-morpholinoethyl) carbodiimide metho-p-toluenesulfonate; OCS, oxidized chondroitin sulfate.

Table S4. Clinical scoring of corneal opacity.

Score	Opacity
0	No corneal opacity
1	1–25% area of corneal opacity
2	26–50% area of corneal opacity
3	51–75% area of corneal opacity
4	76–100% area of corneal opacity

Table S5. Antibody information.

Antibodies	Company	Item No.	Dilution
α-SMA	Abcam	ab7817	1:400
Collagen I	Abcam	ab6308	1:200
CK3	Abcam	ab68260	1:200
CD31	Abcam	ab182981	1:100
CD45	Abcam	ab10558	1:200
ZO-1	Abcam	ab216880	1:200
Laminin	Abcam	ab11575	1:100
Alexa Fluor 594 anti-rabbit	Invitrogen	A21207	1:500
Alexa Fluor 488 anti-rabbit	Invitrogen	A11008	1:500
Alexa Fluor 488 anti-mouse	Invitrogen	A21202	1:500

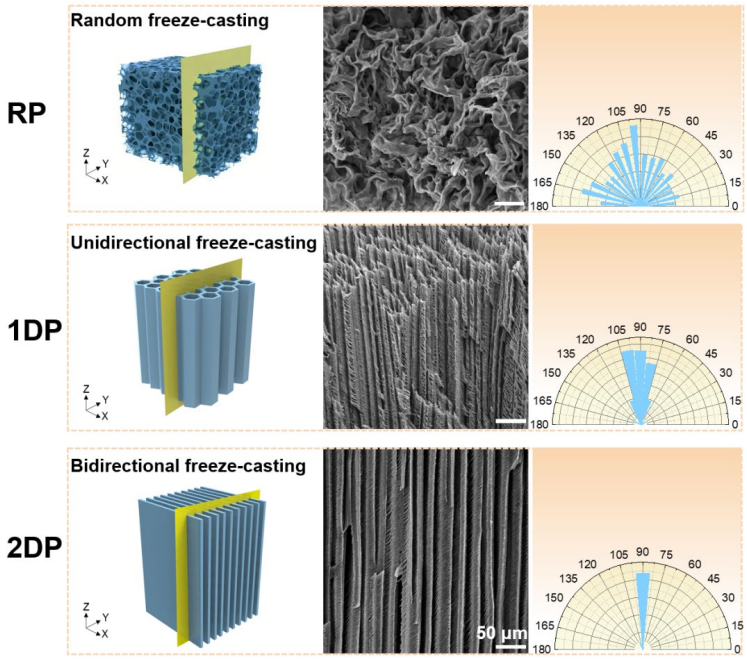


Fig. S1 Morphology of PVA hydrogels by different freezing methods. Schematic diagrams, SEM micrographs, and polar orientation histograms demonstrate that RP features disordered isotropic pores, 1DP has uniaxially aligned pore channels along the freezing direction, and 2DP forms highly ordered lamellar structures (n = 200 measurements per group, randomly collected from multiple SEM fields of view).

.

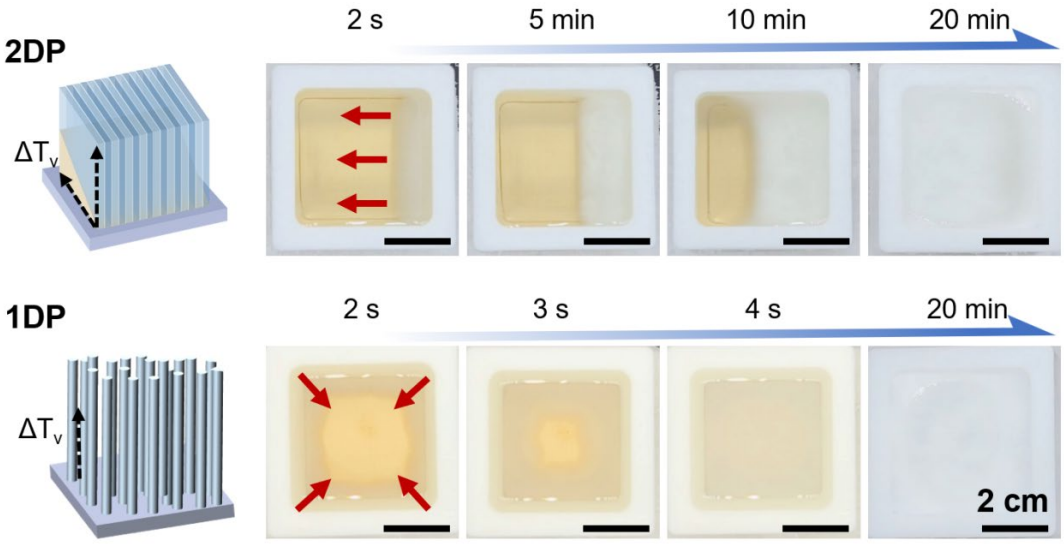


Fig. S2 Dual temperature gradient of 2DP. Schematic illustrations and time-lapse optical images show the slurry freezing progressively along imposed temperature gradients. 2DP ice crystals propagate along dual directions: vertically away from the cold finger and upward along the polydimethylsiloxane wedge, whereas 1DP ice crystals grow exclusively uniaxially perpendicular to the cold finger. Red arrows denote the ice crystal propagation direction.

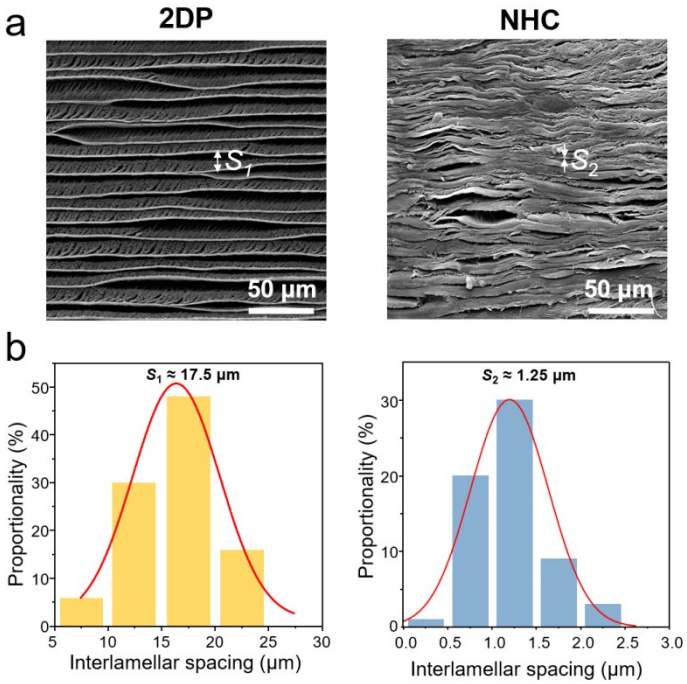


Fig. S3 Characterization of 2DP lamellar spacing. a, SEM images and **b,** interlamellar spacing distribution of 2DP and native human cornea (NHC). (n = 200 measurements per group, randomly collected from multiple SEM fields of view).

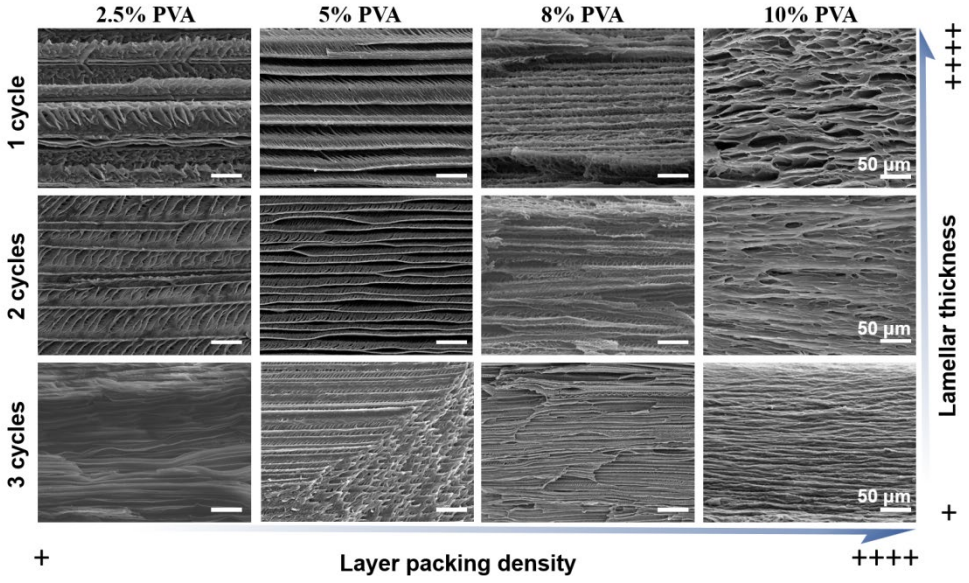


Fig. S4 Tunable lamellar structure of 2DP hydrogels. SEM images demonstrate the evolution of lamellar morphology and microstructure of 2DP hydrogels under varying PVA concentrations and freeze-thaw cycles (+ low, ++++ high).

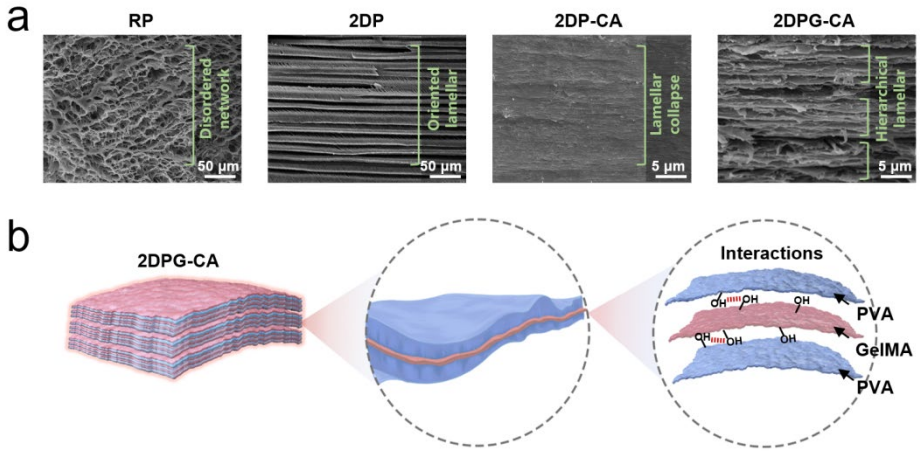


Fig. S5 Contribution of GelMA to hierarchical lamellar structure of 2DPG-CA. a, SEM images of hydrogels: RP exhibits disordered porous networks; 2DP shows aligned lamellae; 2DP-CA displays lamellar collapse and intersheet fusion; 2DPG-CA retains hierarchical lamellar architecture. **b,** Schematic of the 2DPG-CA architecture. A GelMA layer sandwiched between two PVA lamellae acts as an interlayer spacer to prevent lamellar collapse and intersheet fusion upon drying.

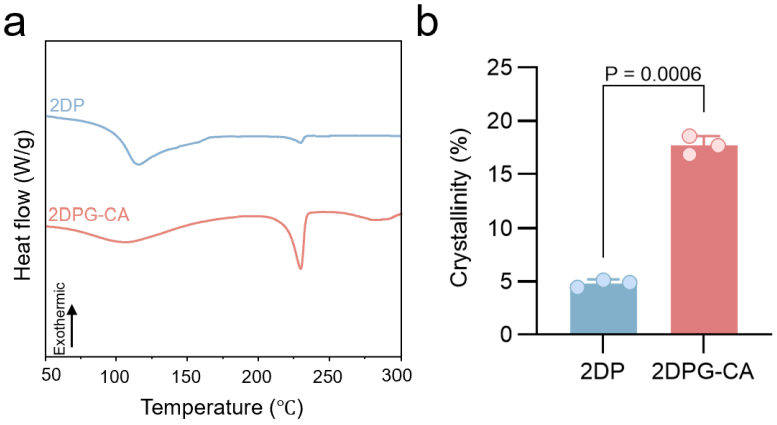


Fig. S6 Effect of omnidirectional confined assembly on hydrogel crystallinity.

a, Differential scanning calorimetry (DSC) curves of 2DP and 2DPG-CA. **b**, Crystallinity quantification. 2DPG-CA exhibits markedly elevated crystallinity (17.7%) versus pristine 2DP (4.8%). Data are presented as the mean ± SD (n = 3 independent samples). Statistical significance in **b** was assessed using a two-sided unpaired Student's t-test; the exact P value is indicated in the panel.

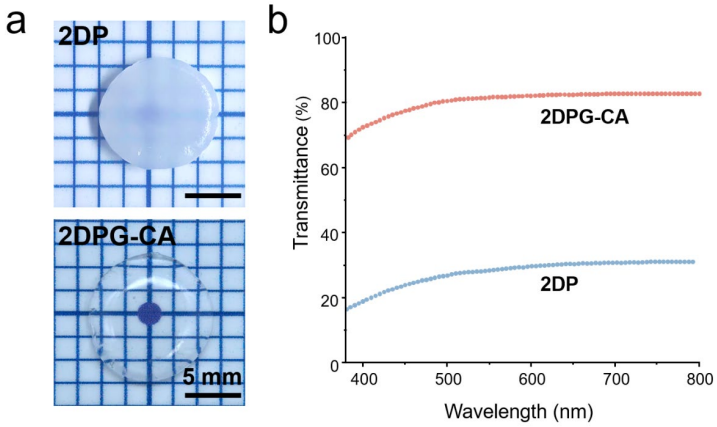


Fig. S7 Optical transmittance of 2DPG-CA. a, Representative optical images comparing visual transparency of 2DP and 2DPG-CA. **b,** UV-vis transmittance spectra over 380–800 nm for both hydrogels.

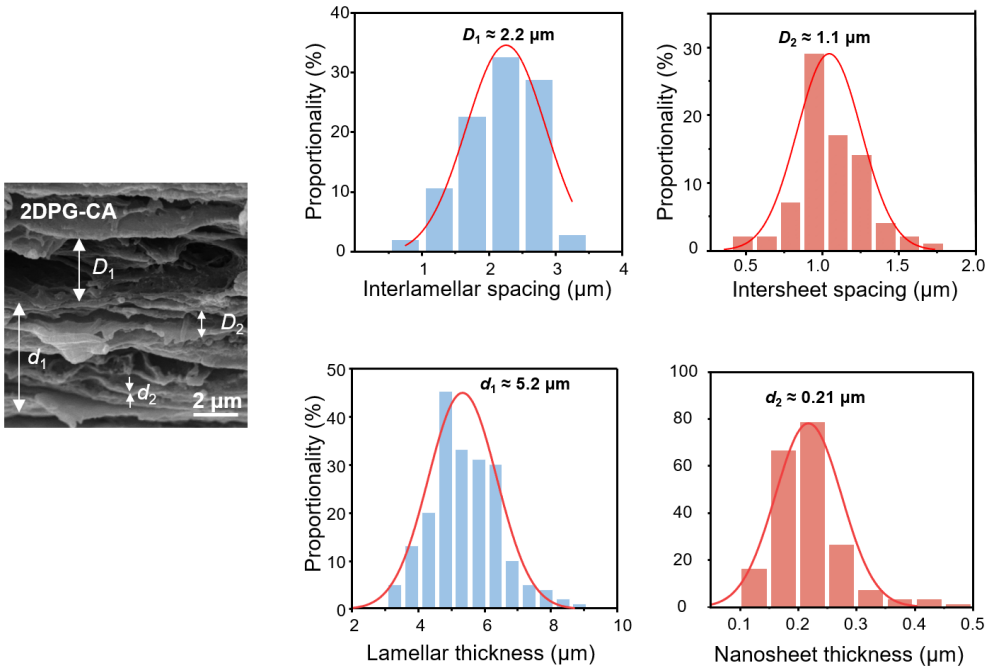


Fig. S8 Hierarchical lamellar structural parameters of 2DPG-CA. SEM image presents the hierarchical lamellar structure of 2DPG-CA. Distribution histograms illustrate the size distributions of lamellar thickness (d_1), interlamellar spacing (D_1), nanosheet thickness (d_2), and intersheet spacing (D_2) (n = 200 measurements per group, randomly collected from multiple SEM fields of view).

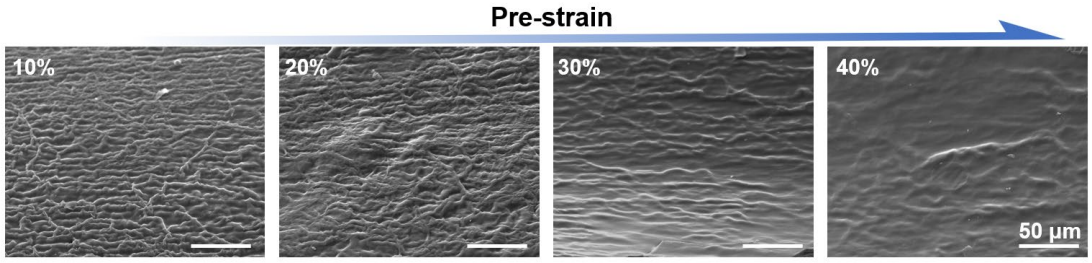


Fig. S9 Surface morphology of 2DPG-CA under varying pre-strain. SEM images of 2DPG-CA hydrogels prepared via confined drying self-assembly under pre-strain of 10%, 20%, 30% and 40%. Prominent lamellar grooves at 10% strain gradually flatten and disappear with increasing strain.

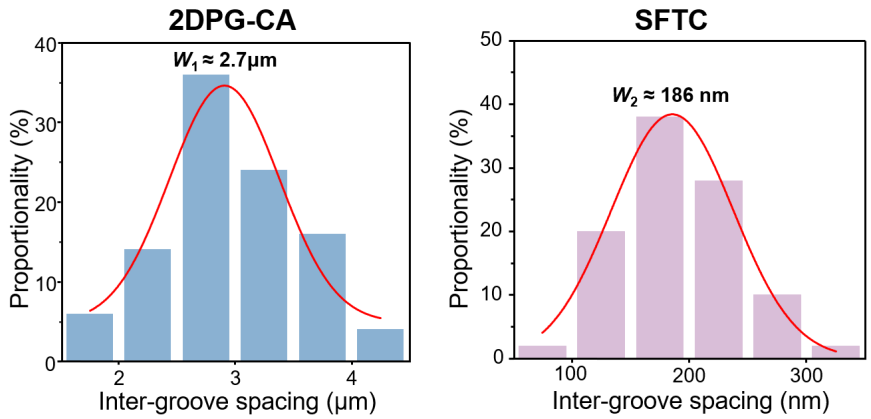


Fig. S10 Inter-groove spacing of 2DPG-CA vs. SFTC. Histograms display the distributions of surface inter-groove spacing, with the average value reduced from ~2.7 μm in 2DPG-CA to ~186 nm in SFTC (n = 200 measurements per group, randomly collected from multiple SEM fields of view).

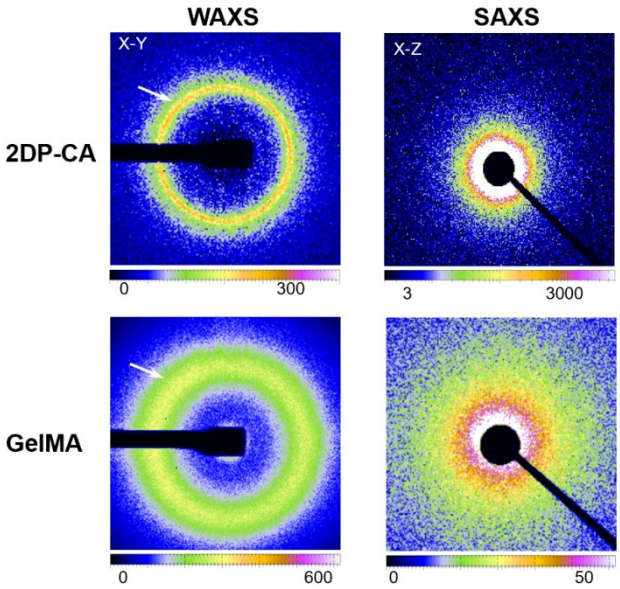


Fig. S11 2D WAXS and SAXS patterns of 2DP-CA and GelMA. Both 2DP-CA and GelMA exhibit isotropic concentric scattering rings in WAXS and SAXS characterizations. The WAXS profile of 2DP-CA shows a sharp diffraction ring originating from PVA crystallites, while GelMA presents a broad amorphous halo (marked by the white arrow).

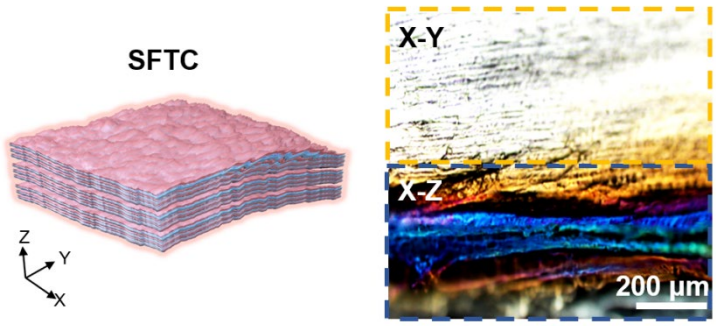


Fig. S12 Polarized optical microscopy (POM) characterization of SFTC.

The schematic illustrates the structural architecture of SFTC, with corresponding POM micrographs showing negligible birefringence in the X–Y in-plane view and distinct interference colors in the X–Z cross-sectional view, verifying the well-aligned lamellar architecture and in-plane isotropy of SFTC.

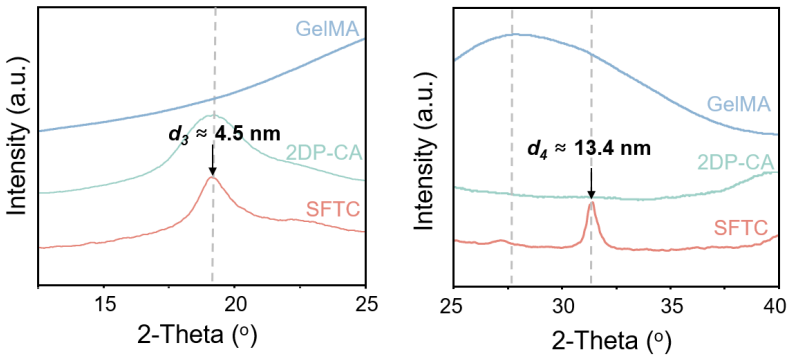


Fig. S13 WAXS characterization of domain sizes. WAXS scattering intensity versus 2θ for GelMA, 2DP-CA and SFTC, ordered domain sizes (d_3, d_4). The unique peak in SFTC lies within the hydrogen bond length range and does not exist in either single component, confirming that it arises from hydrogen-bond-driven ordered packing between PVA and GelMA chains.

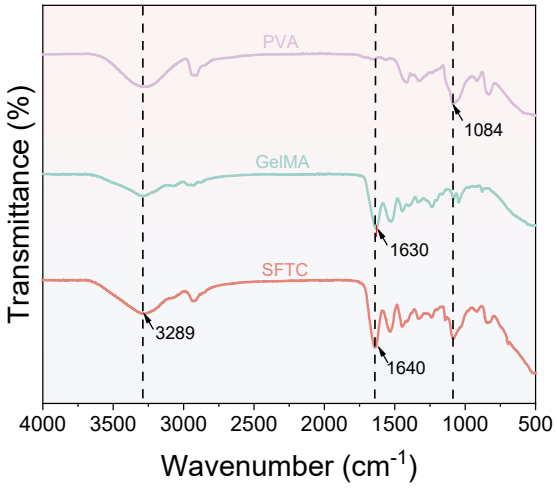


Fig. S14 FTIR of SFTC hydrogel interactions. The SFTC composite retains characteristic peaks of pristine PVA and GelMA without new peak generation. The amide-I/methacryloyl C=C peak of GelMA slightly blue-shifted from 1630 cm^{-1} to 1640 cm^{-1}, with other peaks unchanged. This verifies partial independent photocrosslinking of GelMA within PVA lamellar gaps, while residual GelMA interpenetrates PVA chains via hydrogen-bonding and van der Waals forces to form an interpenetrating network.

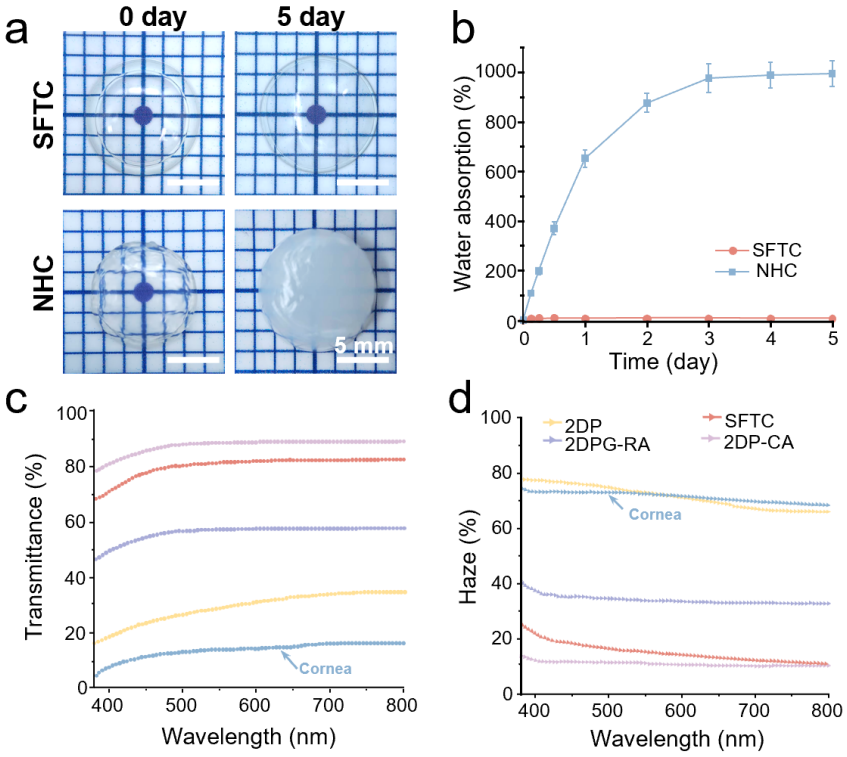


Fig. S15 Hydration stability of SFTC. a) Macroscopic photographs and b) water absorption of SFTC and NHC before and after 5 days of immersion in physiological saline. c) Volume change and d) haze spectra of the hydrogels after 5 days of immersion.

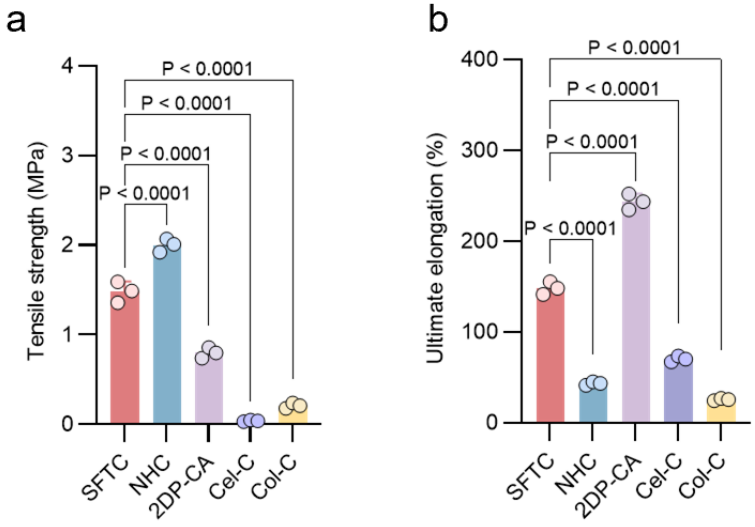


Fig. S16 Mechanical characterization of SFTC. a, Tensile strength and **b**, ultimate elongation of SFTC, NHC, 2DP-CA, Cel-C, and Col-C, data are shown as mean ± s.d. (n = 3 independent samples). Statistical significance for **a** and **b** was assessed using one-way ANOVA followed by Tukey's multiple comparisons test; adjusted P values are indicated in the panels. Unless otherwise specified, all statistical tests were two-sided.

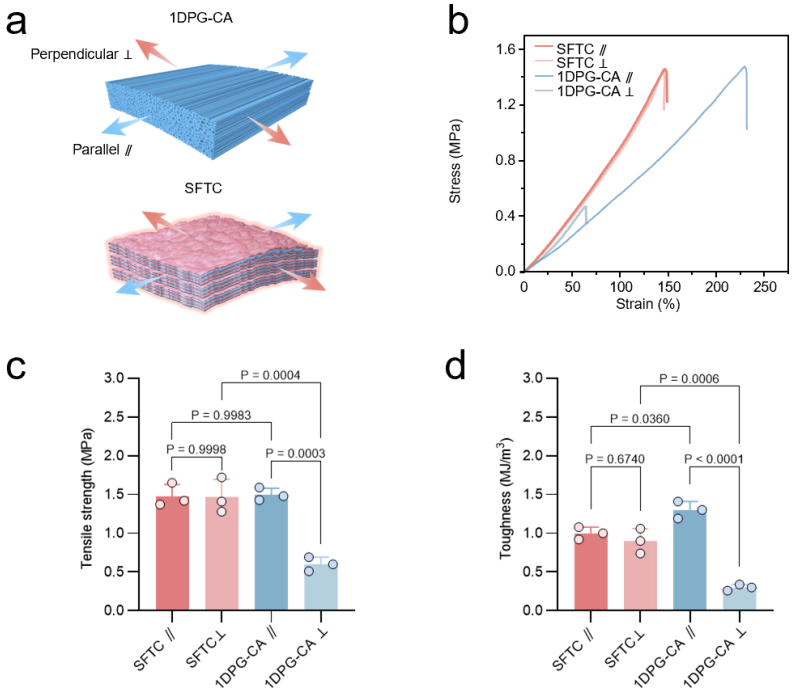


Fig. S17 In-plane isotropic mechanical performance of SFTC. a, Schematic illustrating the two orthogonal tensile loading directions for SFTC and 1DPG-CA

hydrogels. **b**, Stress–strain curves. **c**, Tensile strength and **d**, toughness statistics of both samples along the two orthogonal directions, data are shown as mean ± s.d. (n = 3 independent samples). Statistical significance for **c** and **d** was assessed using one-way ANOVA followed by Tukey's multiple comparisons test; adjusted P values are indicated in the panels. Unless otherwise specified, all statistical tests were two-sided.

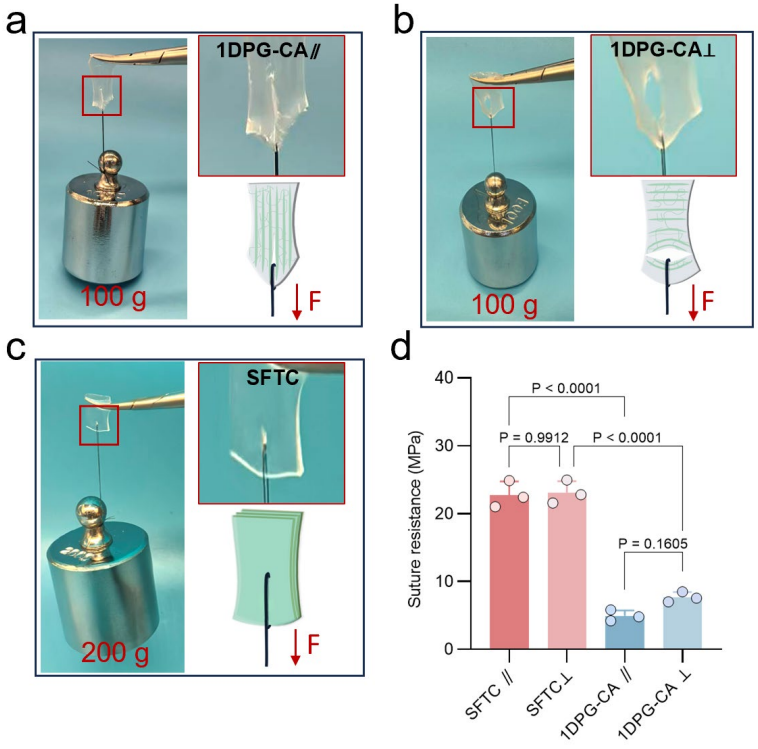


Fig. S18 Isotropic suture retention of SFTC. a, Suture retention tests of 1DPG-CA under 100 g loading show evident tearing in the parallel direction, and **b**, the perpendicular alignment direction. **c**, SFTC withstands a 200 g load without observable tearing. **d**, Quantitative comparison of suture retention strength between SFTC and 1DPG-CA along two orientations, data are shown as mean ± s.d. (n = 3 independent samples). Statistical significance in **d** was assessed using one-way ANOVA followed by Tukey's multiple comparisons test; adjusted P values are indicated in the panel. Unless otherwise specified, all statistical tests were two-sided.

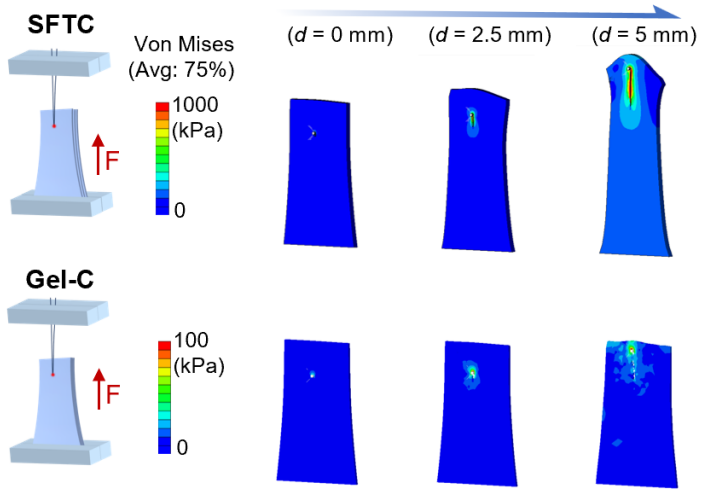


Fig. S19 Mechanics modelling for suture resistance of SFTC. Schematic of the suture tensile setup and Von Mises stress contours at displacements d = 0, 2.5, 5 mm.

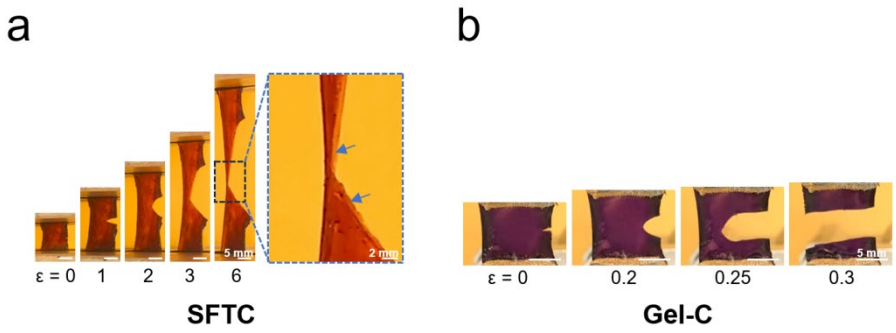


Fig. S20 Notch insensitivity of SFTC. a, Notched SFTC under increasing tensile strain (ε = 0–6). Pronounced crack blunting emerges at the notch tip, which effectively impedes catastrophic crack penetration into the bulk matrix even under large strain. **b,** Notched Gel-C under increasing tensile strain (ε = 0–0.3), featuring rapid crack propagation and catastrophic unstable fracture at low strain. Samples were stained with 0.2% phenol red for visualization.

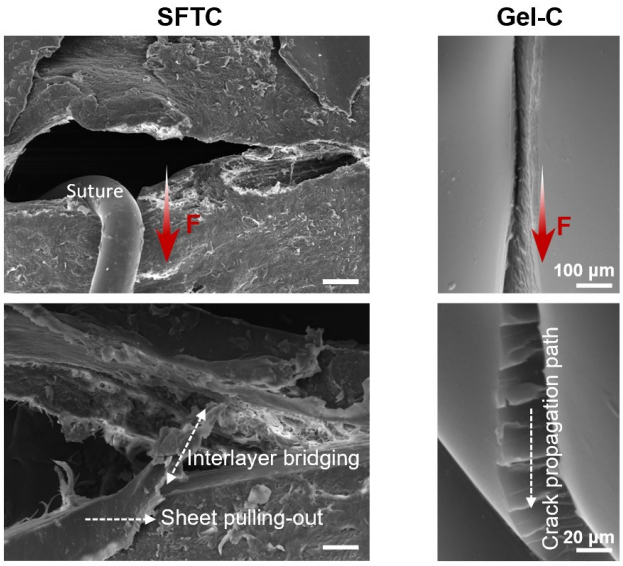


Fig. S21 Suture retention performance of SFTC. SEM images show that under suture loading, the lamellar structure in SFTC exhibits sheet pull-out, and interlayer bridging structures induce crack tip blunting and deflection. Gel-C exhibits typical brittle fracture, with a straight and smooth crack path. Arrows represent the direction of applied stress.

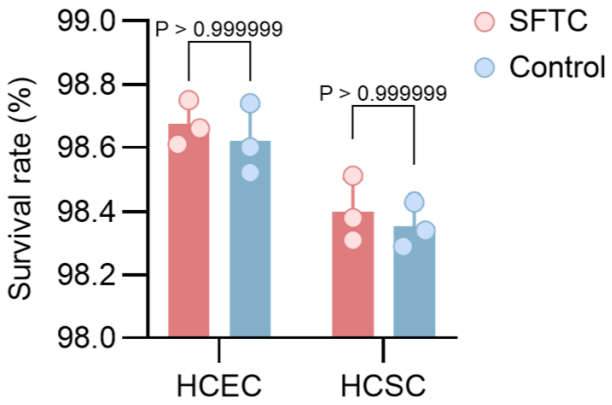


Fig. S22 Quantitative cell viability analysis. Cell viability of HCECs and HCSCs co-cultured with SFTC hydrogels compared with the control group, data are shown as mean ± s.d. (n = 3 independent biological replicates). Statistical significance was assessed using two-sided unpaired Student's *t*-tests for each cell type; exact *P* values are indicated in the panel. Unless otherwise specified, all statistical tests were two-sided.

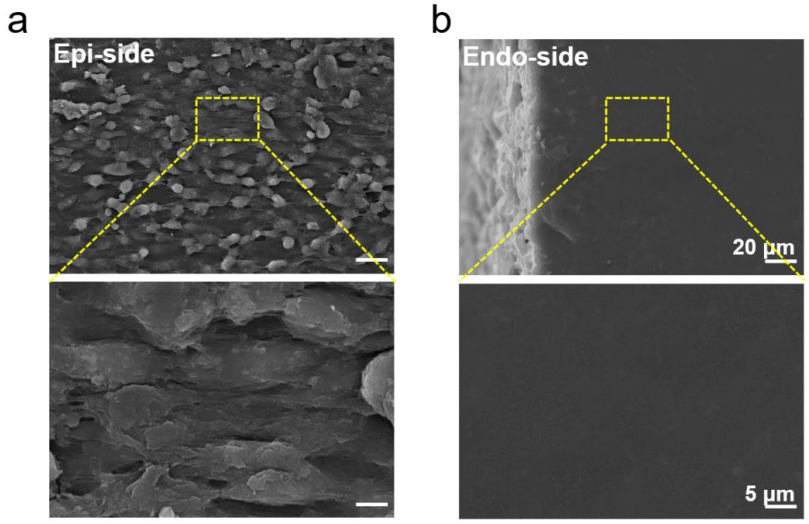


Fig. S23 Asymmetric Cell Adhesion of SFTC. a, SEM images reveal that abundant HCSCs adhere and display oriented spreading on the epi-side (epithelial-facing surface) of the SFTC scaffold. **b,** The endo-side (smooth mold-contacting surface) of the SFTC scaffold exhibits limited cell adhesion.

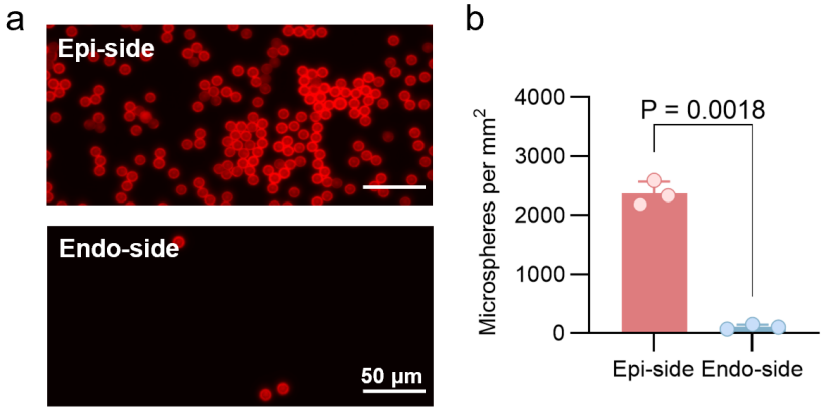


Fig. S24 Asymmetric fibrin microsphere adhesion of SFTC. a, Confocal fluorescence images showing adherent fluorescent fibrin microspheres on the epi- and endo-sides of SFTC. **b**, Quantification of adhesion density on the epi- and endo-sides of SFTC, data are shown as mean ± s.d. (n = 3 independent samples). Statistical significance in **b** was assessed using a two-sided unpaired Student's t-test; the exact P value is indicated in the panel. Unless otherwise specified, all statistical tests were two-sided.

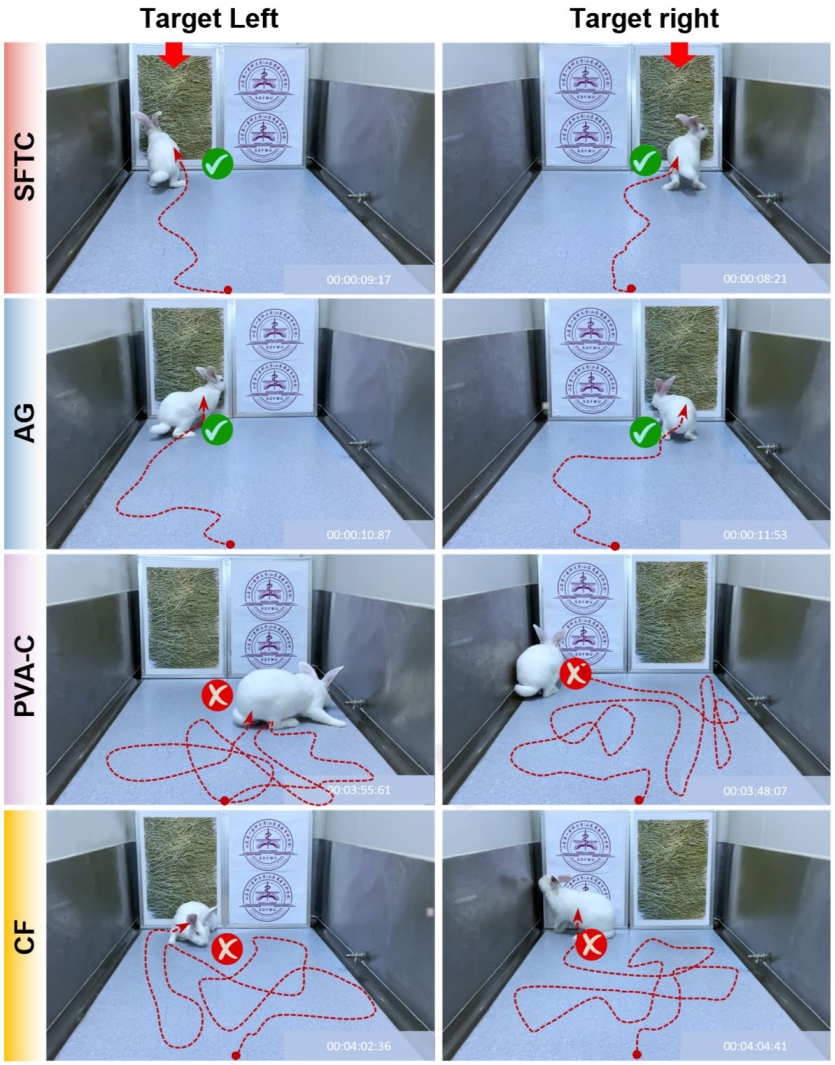


Fig. S25 Functional visual recovery performance of SFTC. Representative foraging trajectories from the cross-modal foraging paradigm. Red arrows indicate the location of the Timothy hay target, positioned on either the left or right side of the test arena. SFTC rabbits exhibit path lengths comparable to the allogeneic graft (AG) group, and significantly shorter than all other control groups. Green checkmarks denote successful foraging; red crosses denote failure.

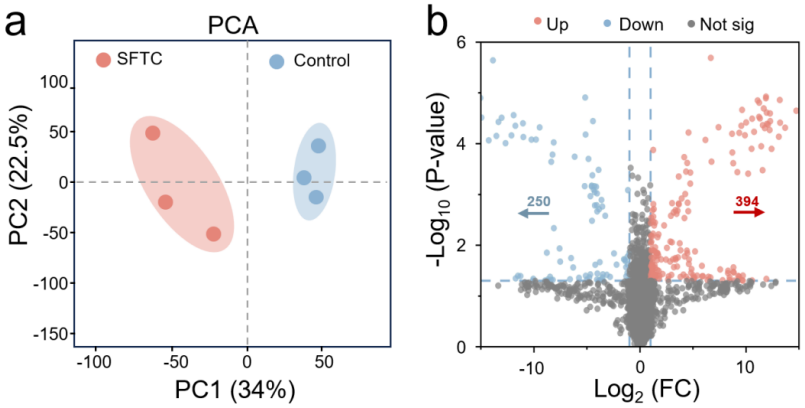


Fig. S26 Proteomic analysis of SFTC and PVA-C transplant groups. a, Principal component analysis (PCA) plot of proteomic data. PC, principal component. **b,** Volcano plot identifying 394 upregulated and 250 downregulated proteins in SFTC relative to PVA-C. FC, fold change.

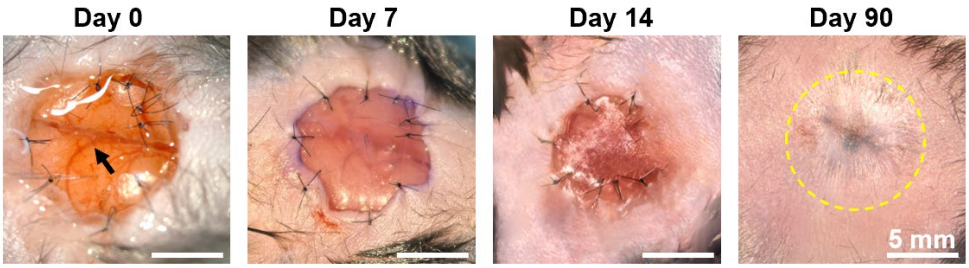


Fig. S27 SFTC for skin regeneration. Representative images of SFTC-repaired full-thickness scalp skin defects in mice over 90 days. The transparent SFTC hydrogel allows clear and real-time observation of the underlying subcutaneous vascular network (marked by the black arrow). Gradual skin healing is observed in mice over the 90-day follow-up period; the yellow dashed circle marks the repaired area.

3. References:

1. Bakhshandeh, H. et al. Poly(ε-caprolactone) nanofibrous ring surrounding a polyvinyl alcohol hydrogel for the development of a biocompatible two-part artificial cornea. *Int. J. Nanomed.* **6**, 1509–1515 (2011).
2. Rafat, M. et al. Bioengineered corneal tissue for minimally invasive vision restoration in advanced keratoconus in two clinical cohorts. *Nat. Biotechnol.* **41**, 70–81 (2023).
3. Shekhawat, N. S., Kaur, B., Edalati, A., Abousy, M. & Eghrari, A. O. Tenon patch graft with vascularized conjunctival flap for management of corneal perforation. *Cornea* **41**, 1465–1470 (2022).
4. Eaton, J. S., Miller, P. E., Bentley, E., Thomasy, S. M. & Murphy, C. J. The SPOTS System: an ocular scoring system optimized for use in modern preclinical drug development and toxicology. *J. Ocul. Pharmacol. Ther.* **33**, 718–734 (2017).
5. Dohlman, C. The Boston keratoprosthesis—the first 50 years: some reminiscences. *Annu. Rev. Vision Sci.* **8**, 1–32 (2022).
6. Priddy, J., Bardan, A. S., Tawfik, H. S. & Liu, C. Systematic review and meta-analysis of the medium- and long-term outcomes of the Boston Type 1 keratoprosthesis. *Cornea* **38**, 1465–1473 (2019).
7. Lee, R. et al. Long-term visual outcomes and complications of Boston keratoprosthesis Type II implantation. *Ophthalmology* **124**, 27–35 (2017).
8. Hicks, C. R. et al. AlphaCor™ cases: comparative outcomes. *Cornea* **22**, 583–590 (2003).
9. Chirila, T. V. An overview of the development of artificial corneas with porous skirts and the use of PHEMA for such an application. *Biomaterials* **22**, 3311–3317 (2001).
10. Moshirfar, M. et al. The historical development and an overview of contemporary keratoprostheses. *Surv. Ophthalmol.* **67**, 1175–1199 (2022).
11. Wang, Q. et al. Mihe (MIOK) KPro with auricular cartilage reinforcement in end-stage corneal blindness: an open-label, nonrandomized trial. *Adv. Ophthalmol. Pract. Res.* **6**, 80–86 (2026).
12. Zhang, T. et al. A multicenter clinical trial of collar-button type keratoprosthesis implantation for the treatment of corneal blindness in high-risk transplantation. *Zhonghua Yan Ke Za Zhi* **59**, 262–271 (2023).
13. Basu, S. et al. The Aurolab Keratoprosthesis (KPro) versus the Boston Type I Kpro: 5-year clinical outcomes in 134 cases of bilateral corneal blindness. *Am. J. Ophthalmol.* **205**, 175–183 (2019).
14. Shanbhag, S. S., Senthil, S., Mohamed, A. & Basu, S. Outcomes of the Boston type 1 and the Aurolab keratoprosthesis in eyes with limbal stem cell deficiency. *Br. J. Ophthalmol.* **105**, 473–478 (2021).
15. Wang, L. Q. et al. Long-term outcomes of the MICOF keratoprosthesis surgery. *Ocul. Surf.* **21**, 178–185 (2021).
16. Huang, Y. F. et al. Moscow eye microsurgery complex in Russia keratoprosthesis in Beijing. *Ophthalmology* **118**, 41–46 (2011).
17. Bakshi, S. K., Paschalis, E. I., Graney, J. & Chodosh, J. Lucia and beyond: development of an affordable keratoprosthesis. *Cornea* **38**, 492–497 (2019).

18. Ortiz-Morales, G. et al. Results of Lucia keratoprosthesis implantation in severe corneal disease. *Am. J. Ophthalmol.* **268**, 388–394 (2024).
19. Litvin, G., Klein, I., Litvin, Y., Klaiman, G. & Nyska, A. CorNeat KPro: ocular implantation study in rabbits. *Cornea* **40**, 1165–1174 (2021).
20. Bahar, I., Reitblat, O., Livny, E. & Litvin, G. The first-in-human implantation of the CorNeat keratoprosthesis. *Eye* **37**, 1331–1335 (2023).
21. Hollick, E. J., Watson, S. L., Dart, J. K. G., Luthert, P. J. & Allan, B. D. S. Legeais BioKpro III keratoprosthesis implantation: long term results in seven patients. *Br. J. Ophthalmol.* **90**, 1146–1151 (2006).
22. Li, G. et al. Design and biocompatibility of a novel, flexible artificial cornea. *Transl. Vis. Sci. Technol.* **13**, 19 (2024).
23. Pan, J. et al. Arrested phase separation enables high-performance keratoprostheses. *Adv. Mater.* **35**, 2207750 (2023).
24. Zhao, L. et al. Natural dual-crosslinking bioadhesive hydrogel for corneal regeneration in large-size defects. *Adv. Healthc. Mater.* **11**, 2201576 (2022).
25. Li, H. et al. Natural cross-linker-stabilized acellular porcine corneal stroma for lamellar keratoplasty. *Acta Biomater.* **114**, 270–284 (2020).
26. Wilson, A., Jones, J. & Marshall, J. Biomechanical evaluation of decellularized and crosslinked corneal implants manufactured from porcine corneas as a treatment option for advanced keratoconus. *Front. Bioeng. Biotechnol.* **10**, 862969 (2022).
27. Shi, W. Y. et al. Protectively decellularized porcine cornea versus human donor cornea for lamellar transplantation. *Adv. Funct. Mater.* **29**, 1902491 (2019).
28. Dong, M. C. et al. Rapid porcine corneal decellularization through the use of sodium N-lauroyl glutamate and supernuclease. *J. Tissue Eng.* **10**, 2041731419875876 (2019).
29. Zhao, L. et al. Corneal stromal structure replicating humanized hydrogel patch for sutureless repair of deep anterior-corneal defect. *Biomaterials* **313**, 122754 (2025).
30. Zhang, Y. Y. et al. Tissue-engineered corneal endothelial sheets using ultrathin acellular porcine corneal stroma substrates for endothelial keratoplasty. *ACS Biomater. Sci. Eng.* **8**, 1301–1311 (2022).
31. Zhao, L. et al. Natural extracellular matrix scaffold-based hydrogel corneal patch with temperature and light-responsiveness for penetrating keratoplasty and sutureless stromal defect repair. *Adv. Healthc. Mater.* **14**, 2402567 (2025).
32. Zhang, C. W. et al. Construction of tissue-engineered full-thickness cornea substitute using limbal epithelial cell-like and corneal endothelial cell-like cells derived from human embryonic stem cells. *Biomaterials* **124**, 180–194 (2017).
33. Sun, X. L. et al. Bioinspired tissue transparency: achieving sclera-to-cornea transplantation. *Adv. Sci.* **13**, e14871 (2026).
34. Zhao, L. et al. Artificial cornea substitute based on hydrogel skeletons with natural stromal hierarchical structure and extracellular matrix for sutureless transplantation. *Adv. Sci.* **12**, 2411540 (2025).
35. Tjoa, K. et al. Mechanical, optical, chemical, and biological evaluations of fish scale-derived scaffold for corneal replacements: a systematic review. *Int. J. Biol. Macromol.* **267**, 131183 (2024).

36. Yin, Y. et al. Highly transparent and elastic acellular swim bladder with potential application in cornea implantation. *J. Mater. Chem. B* **13**, 6689–6700 (2025).
37. Sun, X. L. et al. Application of decellularized porcine sclera in repairing corneal perforations and lamellar injuries. *ACS Biomater. Sci. Eng.* **8**, 5295–5306 (2022).
38. Chen, S. C. et al. Use of fish scale-derived BioCornea to seal full-thickness corneal perforations in pig models. *PLoS One* **10**, e0143511 (2015).
39. Kang, H. H. et al. Decellularized squid mantle scaffolds as tissue-engineered corneal stroma for promoting corneal regeneration. *Bioeng. Transl. Med.* **8**, e10531 (2023).
40. van Essen, T. H. et al. A fish scale-derived collagen matrix as artificial cornea in rats: properties and potential. *Invest. Ophthalmol. Vis. Sci.* **54**, 3224–3233 (2013).
41. Nie, X. et al. 3D-bioprinted biomimetic epithelial-stromal hydrogel construct with in situ photocrosslinkable bioadhesive for suture-free corneal regeneration. *Adv. Healthc. Mater.* **15**, e04578 (2025).
42. Duan, X. & Sheardown, H. Dendrimer crosslinked collagen as a corneal tissue engineering scaffold: mechanical properties and corneal epithelial cell interactions. *Biomaterials* **27**, 4608–4617 (2006).
43. Wu, K. et al. Glycerol modulated collagen fibril evolution and lamellar organization for biomimetic corneal substitutes construction. *Small* **21**, 2407606 (2024).
44. Lei, M. et al. Engineering a functionality-integrated artificial cornea stromal substitute: Janus bio-adhesive implant with a collagen-based multi-scale biomimetic skeleton. *Bioact. Mater.* **51**, 740–757 (2025).
45. Long, K. et al. Improving the mechanical properties of collagen-based membranes using silk fibroin for corneal tissue engineering. *J. Biomed. Mater. Res. Part A* **103**, 1159–1168 (2014).
46. Rafat, M. et al. PEG-stabilized carbodiimide crosslinked collagen–chitosan hydrogels for corneal tissue engineering. *Biomaterials* **29**, 3960–3972 (2008).
47. Ahn, J.-I. et al. Crosslinked collagen hydrogels as corneal implants: effects of sterically bulky vs. non-bulky carbodiimides as crosslinkers. *Acta Biomater.* **9**, 7796–7805 (2013).
48. Lei, M. et al. Electrical signal initiates kinetic assembly of collagen to construct optically transparent and geometry customized artificial cornea substitutes. *ACS Nano* **16**, 10632–10646 (2022).
49. Kong, B. et al. Fiber reinforced GelMA hydrogel to induce the regeneration of corneal stroma. *Nat. Commun.* **11**, 1435 (2020).
50. McTiernan, C. D. et al. LiQD Cornea: pro-regeneration collagen mimetics as patches and alternatives to corneal transplantation. *Sci. Adv.* **6**, eaba2187 (2020).
51. Qian, Y. A. et al. Dopamine-based high-transparent hydrogel as bioadhesive for sutureless ocular tissue repair. *Adv. Funct. Mater.* **33**, 2300707 (2023).
52. Yan, Y. et al. Preparation and in vitro characterization of gelatin methacrylate for corneal tissue engineering. *Tissue Eng. Regen. Med.* **19**, 59–72 (2021).
53. Namli, I. et al. Progressive insights into 3D bioprinting for corneal tissue restoration. *Adv. Healthc. Mater.* **15**, e03372 (2026).
54. Sani, E. S. et al. Sutureless repair of corneal injuries using naturally derived bioadhesive hydrogels. *Sci. Adv.* **5**, eaav1281 (2019).

55. Wang, Q. et al. Photocurable and temperature-sensitive bioadhesive hydrogels for sutureless sealing of full-thickness corneal wounds. *Small Methods* **8**, 2300996 (2024).
56. Li, M. et al. A “T.E.S.T.” hydrogel bioadhesive assisted by corneal cross-linking for in situ sutureless corneal repair. *Bioact. Mater.* **25**, 333–346 (2023).
57. Yazdanpanah, G. et al. A light-curable and tunable extracellular matrix hydrogel for in situ suture-free corneal repair. *Adv. Funct. Mater.* **32**, 2113383 (2022).
58. Gonzalez-Andrades, M. et al. Improving the practicality and safety of artificial corneas: pre-assembly and gamma-rays sterilization of the Boston keratoprosthesis. *Ocul. Surf.* **16**, 322–330 (2018).
59. Park, J., Phrueksaudomchai, P. & Cortina, M. S. Retroprosthetic membrane: a complication of keratoprosthesis with broad consequences. *Ocul. Surf.* **18**, 893–900 (2020).
60. Zhou, H. et al. Genipin-crosslinked polyvinyl alcohol/silk fibroin/nano-hydroxyapatite hydrogel for fabrication of artificial cornea scaffolds—a novel approach to corneal tissue engineering. *J. Biomater. Sci. Polym. Ed.* **30**, 1604–1619 (2019).
61. Holland, G. et al. Artificial cornea: past, current, and future directions. *Front. Med.* **8**, 770780 (2021).
62. Alves, A. L. et al. Cell-laden marine gelatin methacryloyl hydrogels enriched with ascorbic acid for corneal stroma regeneration. *Bioengineering* **10**, 62 (2023).
63. Foerster, C. G., Langenbucher, A., Cursiefen, C., Kruse, F. E. & Seitz, B. Delayed epithelial healing after keratoplasty for lattice corneal dystrophy. *Cornea* **26**, 1182–1183 (2007).
64. Wang, X. et al. Multifunctional synthetic Bowman's membrane-stromal biomimetic for corneal reconstruction. *Biomaterials* **241**, 119880 (2020).
65. Borderie, V. et al. Outcome of graft central thickness after penetrating keratoplasty. *Ophthalmology* **112**, 626–633 (2005).
66. Price, M. O. et al. Descemet's stripping automated endothelial keratoplasty outcomes compared with penetrating keratoplasty from the Cornea Donor Study. *Ophthalmology* **117**, 438–444 (2010).
67. Lei, X. et al. Mechanical and optical properties of reinforced collagen membranes for corneal regeneration through polyrotaxane cross-linking. *ACS Appl. Bio Mater.* **2**, 3861–3869 (2019).
68. Li, Q. et al. Photocurable dual-network hydrogels based on natural polymers for sutureless repair of large corneal defects. *Small* **21**, e2500150 (2025).
69. Tonsomboon, K., Strange, D. G. T. & Oyen, M. L. Gelatin nanofiber-reinforced alginate gel scaffolds for corneal tissue engineering. *Proc. Annu. Int. Conf. IEEE Eng. Med. Biol. Soc.* **2013**, 6671–6674 (2013).
70. Tonsomboon, K., Butcher, A. L. & Oyen, M. L. Strong and tough nanofibrous hydrogel composites based on biomimetic principles. *Mater. Sci. Eng. C* **72**, 220–227 (2017).
71. Zhang, H. et al. A dual-layer convex patch based on collagen-gelatin/alginate for corneal stroma defects repair and irregular penetrating injuries healing. *Int. J. Biol. Macromol.* **321**, 146052 (2025).
72. Aghaei-Ghareh-Bolagh, B. et al. Optically robust, highly permeable and elastic protein films that support dual cornea cell types. *Biomaterials* **188**, 50–62 (2019).

73. Farasatkia, A., Kharaziha, M., Ashrafizadeh, F. & Salehi, S. Transparent silk/gelatin methacrylate (GelMA) fibrillar film for corneal regeneration. *Mater. Sci. Eng. C* **120**, 111744 (2021).
74. Wu, Z., Kong, B., Liu, R., Sun, W. & Mi, S. Engineering of corneal tissue through an aligned PVA/collagen composite nanofibrous electrospun scaffold. *Nanomaterials* **8**, 124 (2018).
75. Gong, S. & Bandyopadhyay, S. An equation for Young's modulus in rubber-toughened PMMA as a function of strain rate and rubber content. *J. Reinf. Plast. Compos.* **26**, 147–153 (2007).
76. Xu, W. et al. PCL scaffold combined with rat tail collagen type I to reduce keratocyte differentiation and prevent corneal stroma fibrosis after injury. *Exp. Eye Res.* **217**, 108936 (2022).
77. Rose, J. B. et al. In vitro evaluation of electrospun blends of gelatin and PCL for application as a partial thickness corneal graft. *J. Biomed. Mater. Res. Part A* **107**, 828–838 (2019).